Science Advances
AAAS

advances.sciencemag.org/cgi/content/full/6/48/eabb5367/DC1

Supplementary Materials for

Mixed-dimensional MXene-hydrogel heterostructures for electronic skin sensors with ultrabroad working range

Yichen Cai, Jie Shen, Chi-Wen Yang, Yi Wan, Hao-Ling Tang, Areej A. Aljarb, Cailing Chen, Jui-Han Fu, Xuan Wei, Kuo-Wei Huang, Yu Han, Steven J. Jonas*, Xiaochen Dong*, Vincent Tung*

*Corresponding author. Email: sjjonas@mednet.ucla.edu (S.J.J.); iamxcdong@njtech.edu.cn (X.D.); vincent.tung@kaust.edu.sa (V.T.)

Published 27 November 2020, *Sci. Adv.* **6**, eabb5367 (2020)
DOI: 10.1126/sciadv.abb5367

The PDF file includes:

Other Supplementary Material for this manuscript includes the following:

(available at advances.sciencemag.org/cgi/content/full/6/48/eabb5367/DC1)

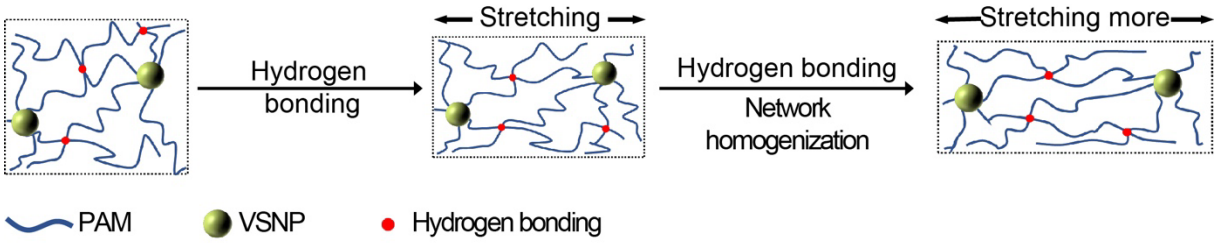

Fig. S1. Schematic of structural configuration inside the modified VSNP-PAM hydrogel networks. Under deformation, physically crosslinked, crystalline microdomains embedded within the VSNP-PAM chains will slip and de-crosslink with hydrogen bonding to dissipate mechanical energy, while maintaining a high elasticity at the same time.

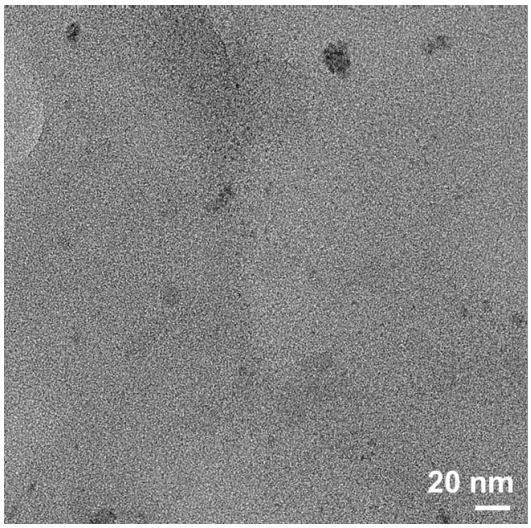

Fig. S2. Transmission electron microscopy (TEM) image showcases the monodispersed vinyl silica nanoparticles (VSNPs).

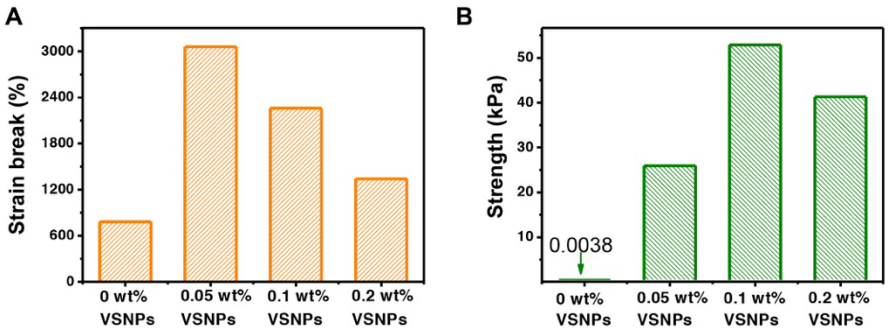

Fig. S3. Comparisons of mechanical properties: strain (A) and tensile strength (B) of VSNP-PAM hydrogels mixed with different concentrations of VSNPs expressed as the weight percent (wt%).

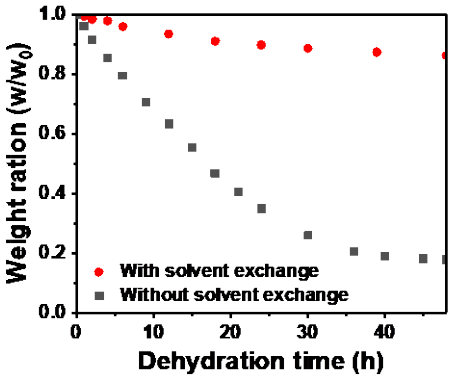

Fig. S4. The VSNP-PAM hydrogel treated with solvent exchange displays less than 15% of loss in its original weight under the ambient testing conditions (24 °C and 60% humidity) for 48 h. Conversely, VSNP-PAM hydrogel without the prior solvent exchange displays more than 80% of loss in its original weight under the same testing conditions.

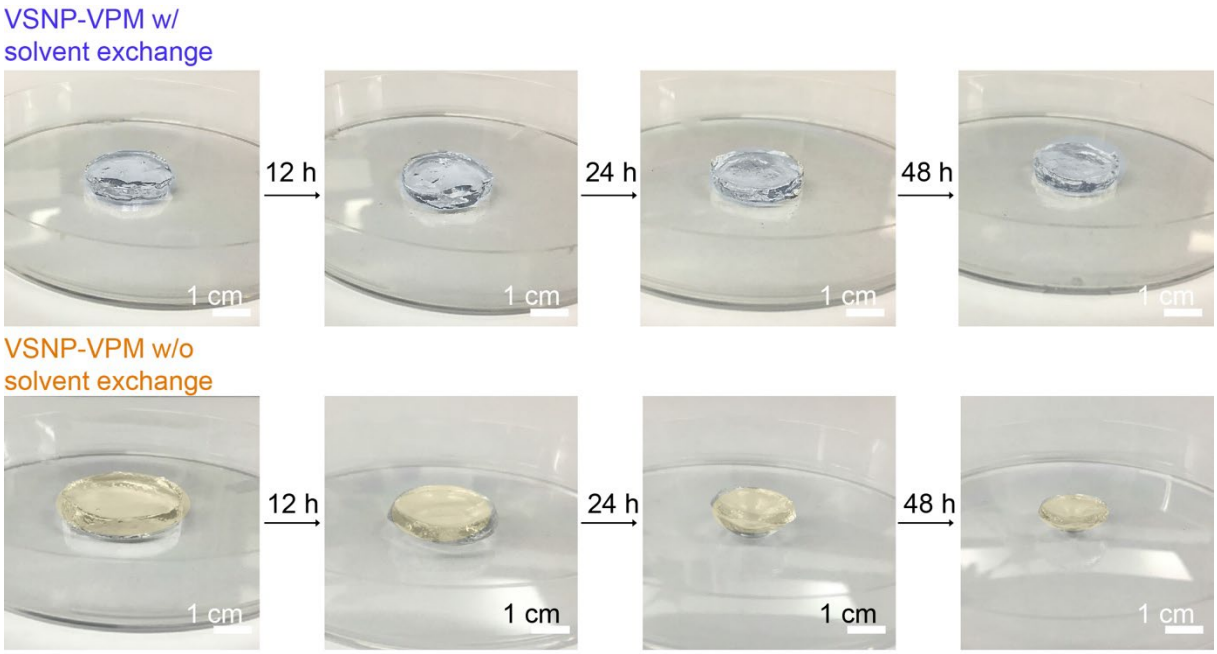

Fig. S5. Snapshots of the VSNP-PAM hydrogel with (top panel) and without solvent exchange (bottom panel) during the dehydration experiments. (Photo credit: Yichen Cai, and Jie Shen, KAUST)

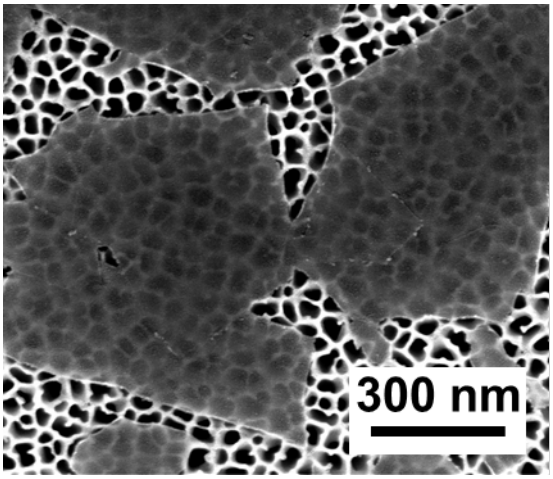

Fig. S6. SEM of MXene flakes on an AAO substrate.

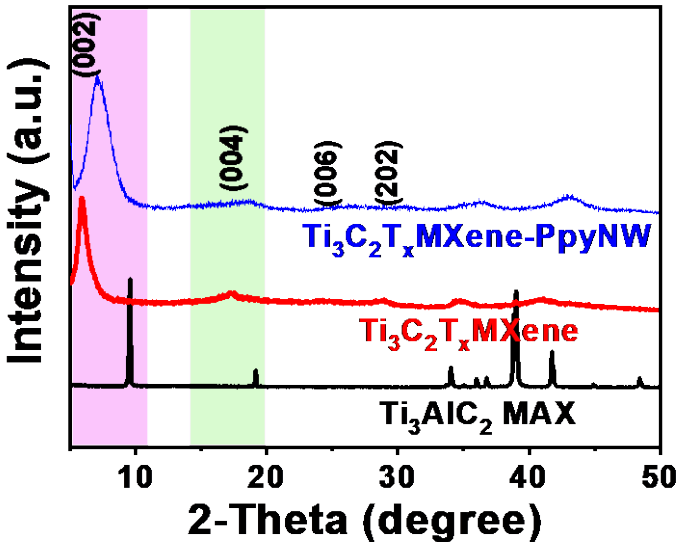

Fig. S7. XRD of Ti_3AlC_2 MAX, $Ti_3C_2T_x$ MXene, and $Ti_3C_2T_x$ MXene-PpyNW, respectively.

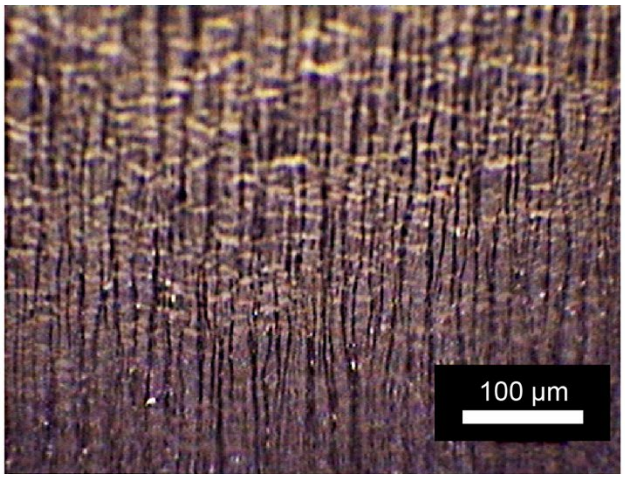

Fig. S8. Real-time observation of the directionally wrinkled e-skin under an optical microscope.

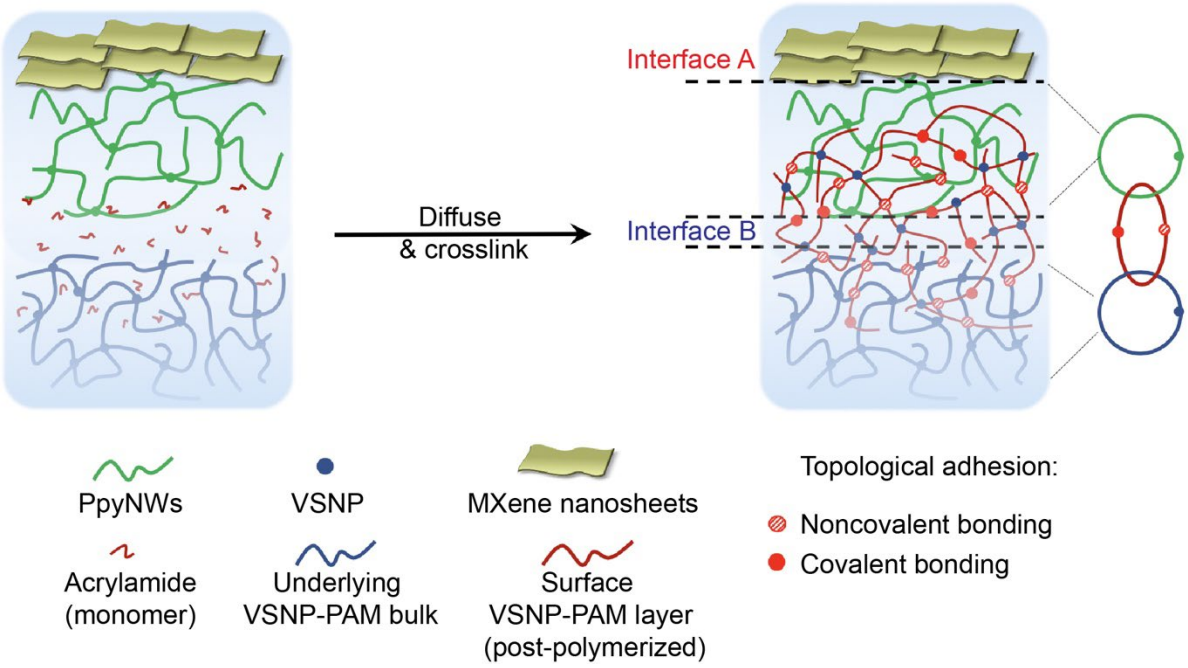

Fig. S9. Schematic illustration shows that the first layer of PpyNW acts like a "double-sided adhesive" to link the MXene with VSNP-PAM hydrogel. Interface A is stabilized by the hydrogen bonding and topological adhesion between PpyNW and VSNP-PAM. An additional layer of acrylamide monomers was deposited prior to the deposition of PpyNW. Upon polymerization, these acrylamide monomers begin to crosslink into and entangle with the VSNP-PAM networks which weaves in and becomes entangled with both PpyNW and VSNP-PAM hydrogel. Interface B is held by the spatially abundant hydrogen bonding between PpyNW and MXene.

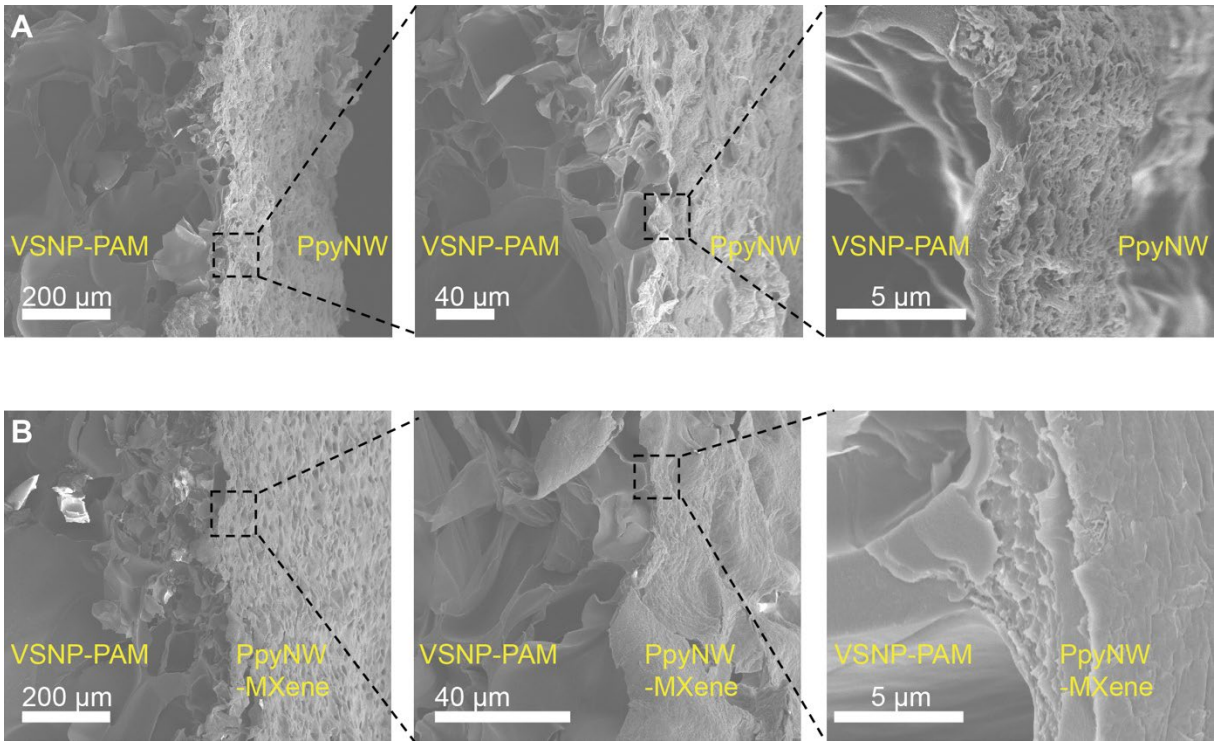

Fig. S10. Engineered interface with PpyNW. Cross-sectional SEM images of PpyNW-VSNP-PAM (A) and MXene-PpyNW-VSNP-PAM (B).

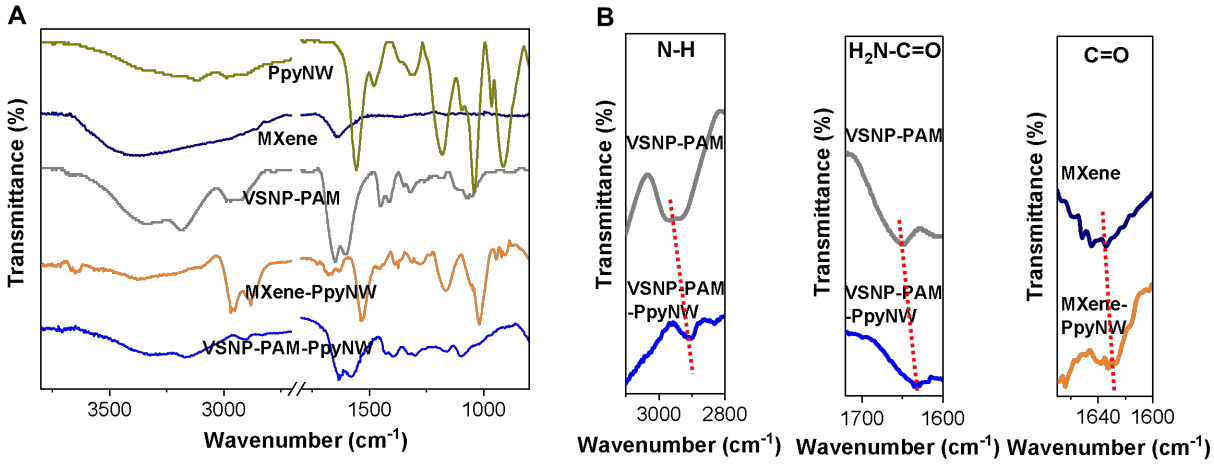

Fig. S11. Crosslinking through hydrogen bonding. (**A**) FTIR spectra of VSNP-PAM hydrogel, PpyNW, MXene, VSNP-PAM-PpyNW composite, and MXene-PpyNW composite. (**B**) Comparison of the characteristic peaks of –NH, H_2N–C=O, and C=O.

FTIR spectra of VSNP-PAM hydrogel, PpyNW, MXene, VSNP-PAM-PpyNW composite, and MXene-PpyNW composite are illustrated in Fig. S11. For VSNP-PAM hydrogel, the observed peaks centered at 3,339 and 3,189 cm^{-1} are attributed to the stretching vibration of –NH from the acrylamide unit. The peak corresponding to H_2N–C=O linkage is localized between 1,600–1,700 cm^{-1}, while the characteristic peak at 1,120 cm^{-1} is assigned to the in-plane rocking of $–NH_2$ (42). For PpyNW, peaks at 1,557 and 1,476 cm^{-1} are due to the antisymmetric and symmetric ring-stretching modes, respectively (43). The broad peak ranging from 3,000 to 3,500 cm^{-1} is attributed to –NH and –CH stretching vibrations. C–N stretching vibration appears at about 1,309 cm^{-1}. –OH and –C=O absorption bands from MXene nanosheets are observed at 3,404 and 1,639 cm^{-1}, respectively (44). All of these results agree well with literature (42-44). We observed the two distinct vibrational modes assigned to N–H (from 2,945 to 2,903 cm^{-1}) and H_2N–C=O (from 1,655 to 1,635 cm^{-1}) along with a significant redshift in the VSNP-PAM-PpyNW composite (45). Similarly, a discernable redshift of –C=O band in MXene-PpyNW sensing layer (from 1,634 to 1,628 cm^{-1}) is also observed. Together, these red shifts in N-H, H_2N–C=O, and –C=O vibrational modes indicate the formation of spatially abundant hydrogen bonding within the interfaces of e-skin.

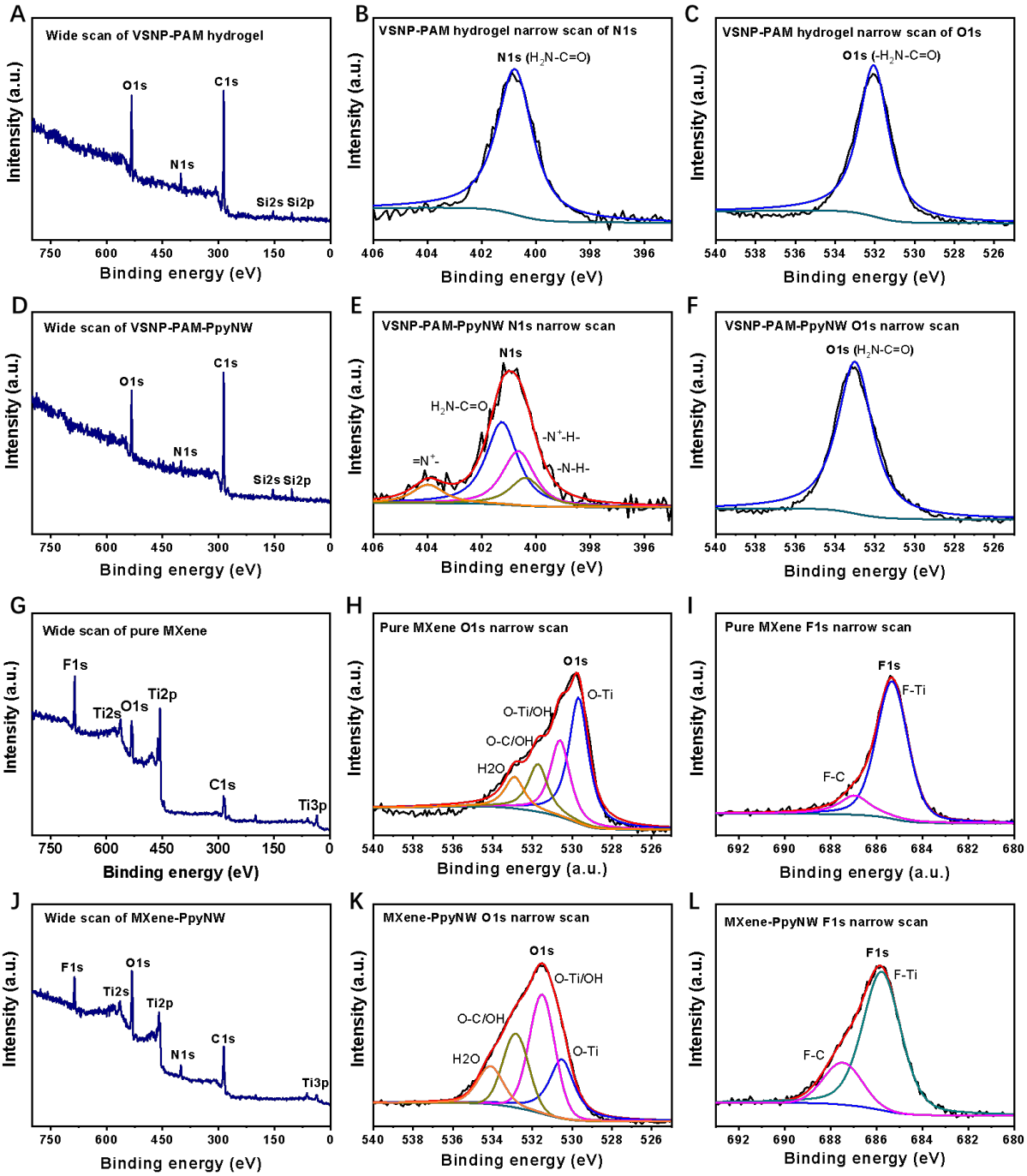

Fig. S12. XPS spectra. (**A-C**) pure VSNP-PAM, (**D-F**) VSNP-PAM-PpyNW composite, (**G-I**) pure MXene and (**J-L**) MXene-PpyNW composite.

Wide scan spectra: A, D, G, and J. Narrow scan of N_{1s}: B and E. Narrow scan of O_{1s}: E, F, H, and K. Narrow scan of F_{1s}: I and L. In order to characterize the hydrogen bonding between MXene, VSNP-PAM and PpyNW, XPS spectra were recorded using monochromatized Al Ka radiation (1486.6 eV). Fig. S12B and C show that pure VSNP-PAM hydrogel has amide functional group of $H_2N{-}C{=}O$, with N_{1s} peak at 400.8 eV and O_{1s} peak at 532.1 eV (46). Adding

PpyNW gives rise to the change of N_{1s} spectra, i.e., three new peaks appear centering at 400.3, 400.6 and 403.8 eV, which are corresponding the benzenoid amine (−NH−), protonation benzenoid amine (−N^+H−), and protonation quinonoid imine (=N^+H−), respectively (47). It is noted that the N_{1s} and O_{1s} peaks shift to 401.3 and 532.9 eV (shown in Fig. S12E and F, and Table. S1). As shown in Fig. S12H, four types of O atoms composed of O_{1s} of pure MXene, which are O-Ti (529.7 eV), O-Ti/OH (530.6 eV), O-C/OH (531.7 eV) and H_2O (532.9 eV), respectively. F_{1s} region is composed of F-Ti (685.3 eV) and F-C (686.8 eV). These results are in consistence with reported works (48, 49). After hybridized with PpyNW, peaks of O-Ti, O-Ti/OH, O-C/OH, F-Ti, and F-C significantly shift to 530.5, 531.4, 532.8, 685.8, and 687.5 eV. All these shifts in the core electrons of individual atoms indicate the decreased electron cloud densities, suggesting that the N and O atoms on hydrogel and O and F atoms on MXene could form hydrogen bonding with –NH groups on PpyNW.

Table. S1. XPS data of pure vinyl hybrid silica nanoparticle modified polyacrylamide (VSNP-PAM) hydrogel and VSNP-PAM-PpyNW composite.

Elements	Groups	PVSNP-AM Hydrogel (eV)	VSNP-PAM-PpyNW (eV)
O_{1S}	$H_2N-C=O$	532.1	532.9
N_{1S}	$H_2N-C=O$	400.8	401.3

Table. S2. XPS data of pure $Ti_3C_2T_x$ MXene and $Ti_3C_2T_x$ MXene-PpyNW composite.

Elements	Groups	Pure MXene (eV)	MXene-PpyNW (eV)
O_{1S}	O-Ti	529.7	530.5
	O-Ti/OH	530.6	531.4
	O-C/OH	531.7	532.8
F_{1S}	F-Ti	685.3	685.8
	F-C	686.8	687.5

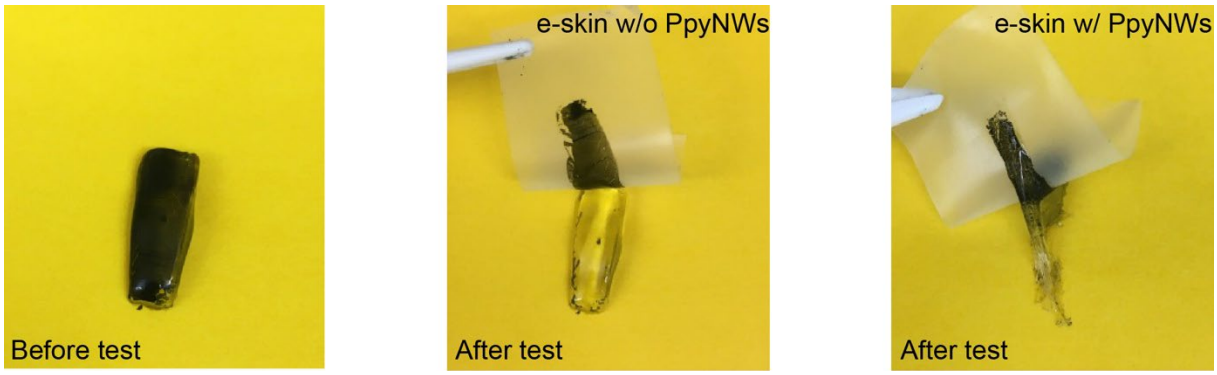

Fig. S13. Photographs showing the different surface adhesion of MXene and MXene-PpyNW composites to VSNP-PAM hydrogels with 3M tape peeling tests. (Photo credit: Yichen Cai, and Jie Shen, KAUST)

Table S3. Comparison between the VSNP-PAM and some representative hydrogel-based sensors

Materials	Strategies	Sensing Type	Working Range	Gauge Factor	Applications
Poly (vinyl alcohol) (PVA)-CNT (*19*)	Embedding, composite	Piezoresistive	0-1,000%	1.5 (1,000% strain)	Strain sensor
Polyvinylpyrrolidone (PVP)-CNC/Fe^{3+}(*50*)	Embedding, composite/network	Piezoresistive	0-1,200%	0.478 (200% strain)	Strain sensor
Poly(acrylamide) (PAAm)-PDMS (*36*)	3D Printing, composite	Piezoresistive	0-200%	0.84 (40% strain)	Strain sensor
Poly(acrylamide) (PAAm)-Graphene (*51*)	Embedding, composite	Piezoresistive	0-1,100%	9 (30% strain)	Strain sensor
κ-carrageenan-PAAm (*52*)	Double-network	Piezoresistive	0-1,000%	0.63 (1,000% strain)	Strain sensor
PVA-$Ti_3C_2T_x$ paste (*17*)	Embedding, composite	Piezoresistive	0-40%	25 (40% strain)	Strain sensor
Amorphous calcium carbonate (ACC)-polyacrylic acid (PAA)- alginate (*53*)	Ionic gel	Capacitive	0-1 kPa	0.17 kPa^{-1}	Pressure sensor
Ag/tannic acid (TA)-CNC (*54*)	Embedding, composite	Piezoresistive& Capacitive	0-400%	9 (30% strain)	Strain sensor
Vinyl hybrid silica nanoparticle (VSNP)-PAM-MXene-Poly pyrrole nanowires **(This work)**	Dynamic interface crosslinking, Pre-strain in both axis	Piezoresistive& Capacitive	0-2,800% 0-30 kPa^{-1} 0-20 cm spatial distance	11.2 (x-direction 1,500%) 16.9 (y-direction 1,500%) 6.74 -0.06 kPa^{-1}	Strain sensor Pressure sensor Tactile sensor

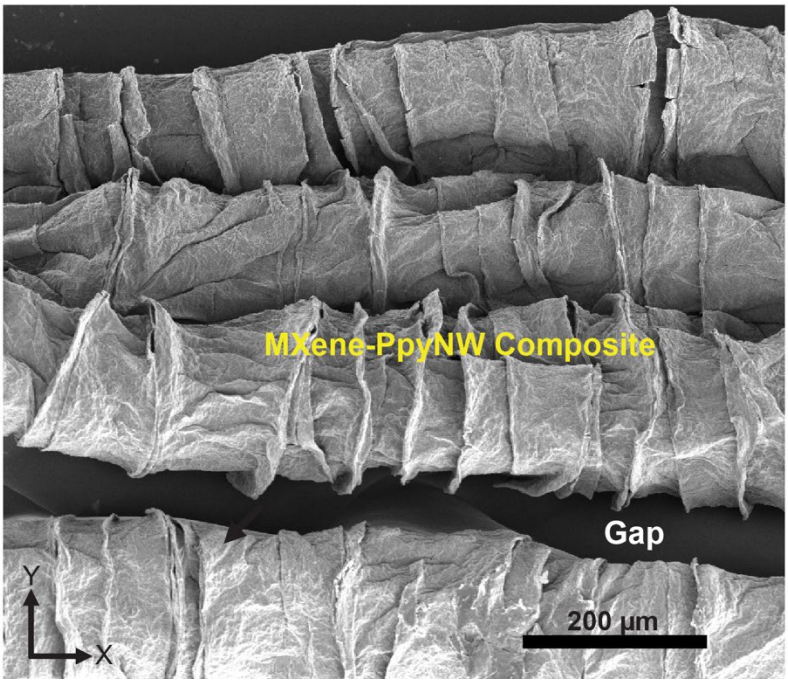

Fig. S14. SEM image of the composite film (MXene-PpyNW) sprayed on pre-stretched VSNP-PAM in x-direction only.

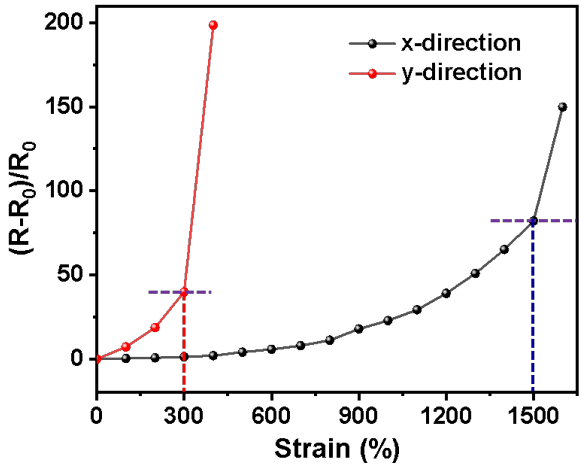

Fig. S15. The relative resistance-strain curves of e-skin sensors based on MXene-PpyNW composites prepared with unidirectional pre-stretching (x-direction only).

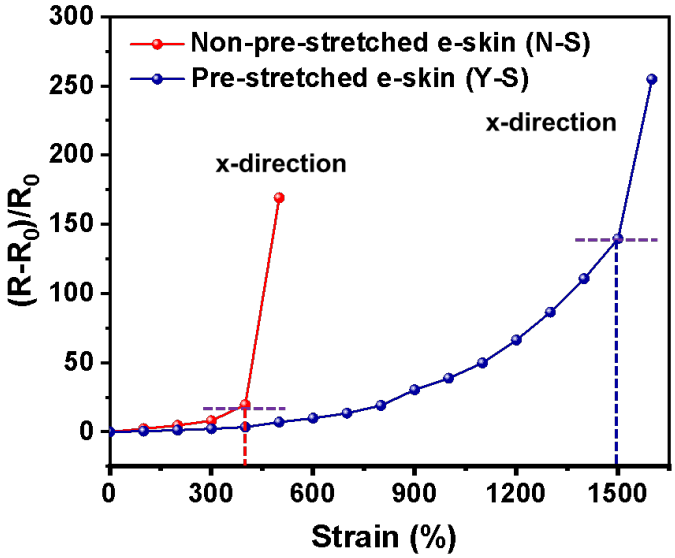

Fig. S16. Relative resistance-strain curves of non-pre-stretched e-skin (N-S) and pre-stretched e-skin (Y-S) at a stretching rate of 5% min^{-1}.

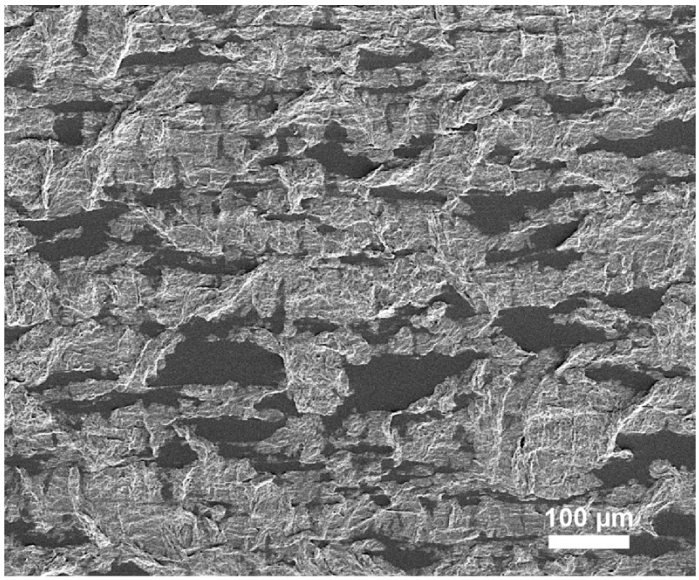

Fig. S17. SEM image of MXene-PpyNW composite film (N-S) shows scattered gaps after several cycles of stretch-release process in the range of 0-500% strain.

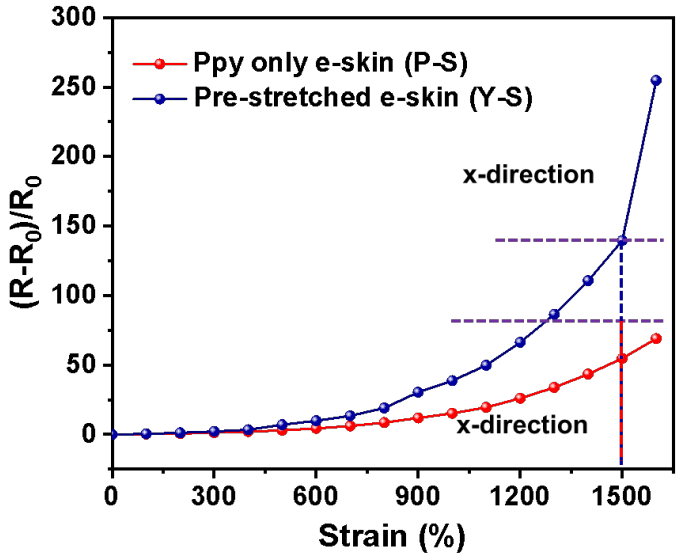

Fig. S18. Relative resistance-strain curves of PpyNW only (P-S) and MXene-PpyNW based (Y-S) e-skin sensors at a stretching rate of 5% min^{-1}.

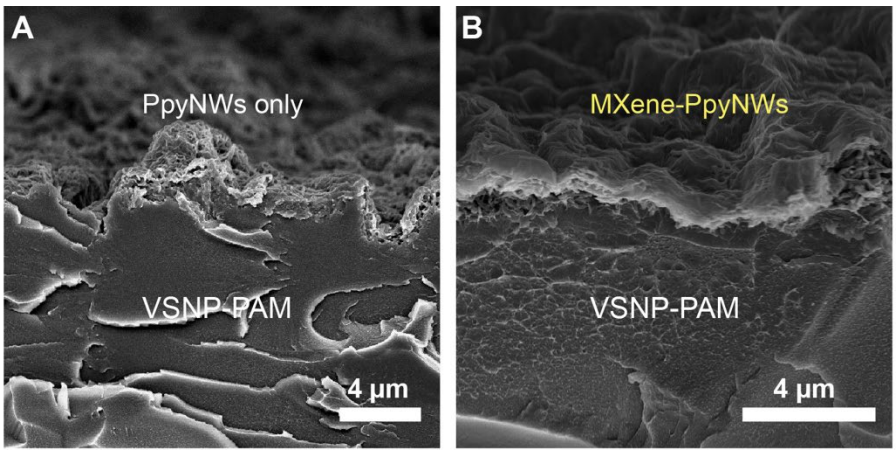

Fig. S19. Cross-section SEM images of (**A**) PpyNW only and (**B**) MXene-PpyNW composite films.

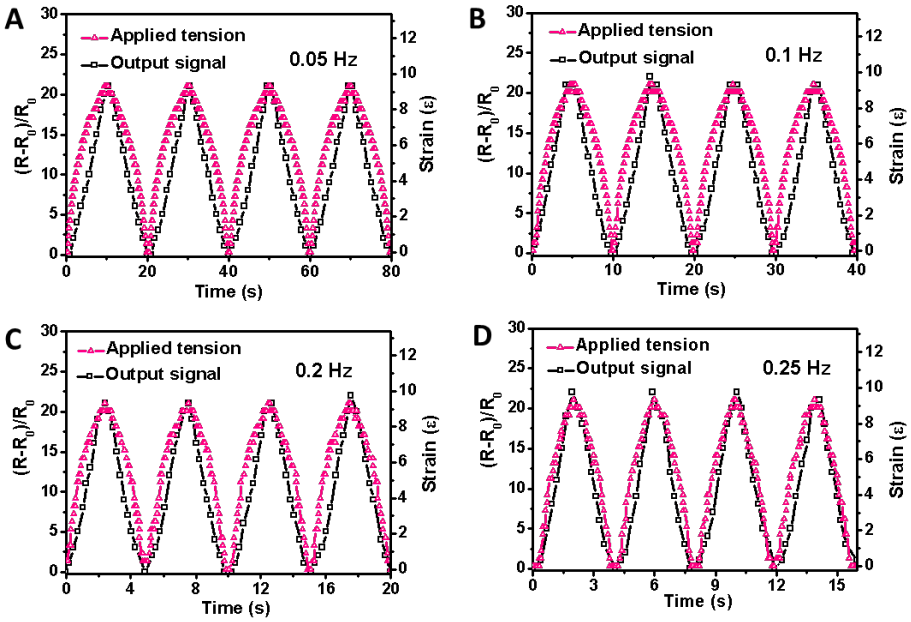

Fig. S20. A-D, Frequency responses of the strain sensor (6 *spray coating cycles*) with strain input frequency 0.05, 0.1, 0.2, and 0.25 Hz, respectively (dynamic strain 1,000%).

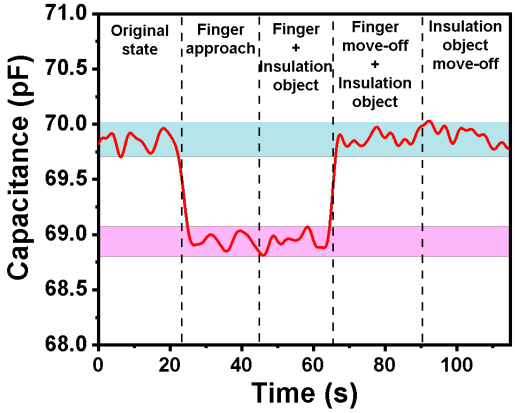

Fig. S21. Capacitances of the e-skin sensor with different approaching conditions by finger and an insulating object.

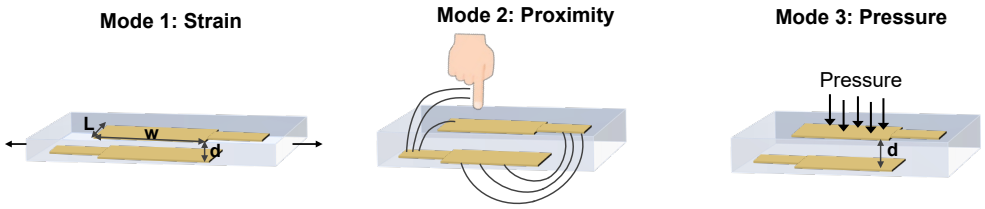

Fig. S22. Stretchable e-skin sensor exhibits three functional modes based on the capacitive sensing mechanisms.

As described in Fig. 5B, three types of capacitances are found to take effect individually or cooperatively when subjected to external stimuli intimately or remotely. They were defined as the plate electrodes capacitance (C_p), the fringing capacitance in the VHB overlay (C_{f1}), and the fringing capacitance through the medium directly above the sensor (C_{f2}), respectively. The sensor capacitance (C_{total}) is the sum of the three capacitances above.

In the strain Mode 1, a large (> 1%) strain is applied to the e-skin as the underlying biological skin stretches. C_p increases with the applied strain as a consequence of an increased surface area of the electrodes, e.g., length (L) × width (W), and a decreased thickness of dielectric layers. Changes in C_{f1} and C_{f2} are negligible compared to C_p. Therefore, increases in the sensor capacitance C_{total} can be directly related to the increasing strain. Because the Mode 1 of capacitive sensing mechanism is not accurate and applicable to large stretching (>1%). In our work, we did not use Mode 1 for strain detecting, which was replaced by piezoresistive sensing for strain detecting as shown in Fig. 4 in the main text.

In the proximity Mode 2, a foreign object, such as the finger, metal, or insulator approaches the e-skin and gently touch the surface without pressure. This in turn disrupts the fringing electric field above the sensor (C_{f2}). Since no geometrical deformation takes places, both C_p and C_{f1} remain constant and changes in C_{total} correspond to C_{f2}. The sensor functions by detecting small changes in the electric field between its top electrode and the object in its proximity. When the foreign object is an earthed, conducting medium (e.g., finger of user), C_{total} decreases with C_{f2} by the charge being grounded through the finger. In parallel, if the approached object is electrically insulating ($\varepsilon > \varepsilon_{air}$), or conducting but ungrounded (larger conducting surface area), C_{total} increases with C_{f2}. The increased C_{total} by the ungrounded object is usually negligible to the decreased C_{total} by the grounded object. Therefore, the stimulus response of sensors in

different surrounding environments can be distinguished.

In the pressure Mode 3, a pressure (P) is applied to the sensor surface, C_p and C_{f1} increase with the reduced distance between the electrodes, arousing the increase of C_{total} (the declined C_{f2} is subtracted). When the pressure continuously increases, the changes of C_p become dominant for C_{total}, back to Mode 1 with strain larger than 1%. A similar mechanism is widely used in the capacitive touch screens (55). Exploiting this proximity and pressure sensory capabilities coupled with the strain sensing provides prospects for area adjustability and expandability for multi-stimulus sensing.

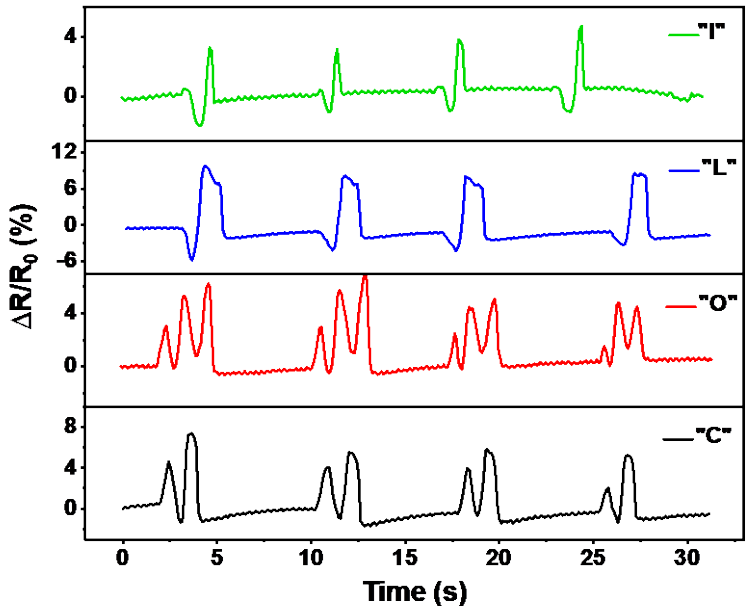

Fig. S23. Recognition of handwriting letters: “C”, “O”, “L”, and “I” with same strokes.

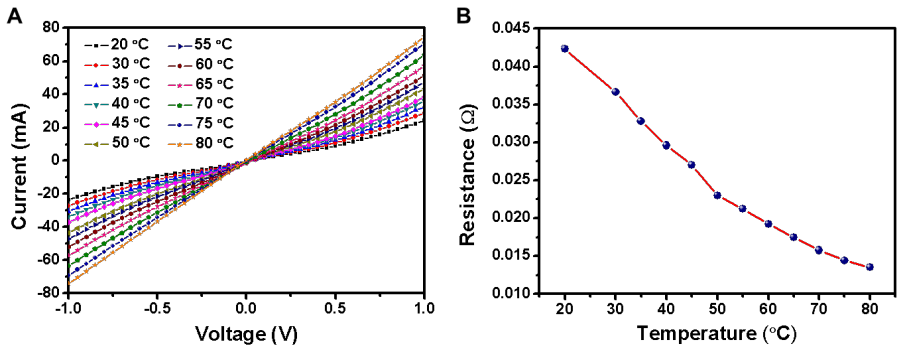

Fig. S24. Current-voltage curves of the e-skin sensor at different temperatures ranging from 20 to 80 °C. MXene-PpyNW-VSNP-PAM based sensory system with a sensing capability for temperature variation enables e-skins to communicate feelings through a skin-to-skin contact physiologically.

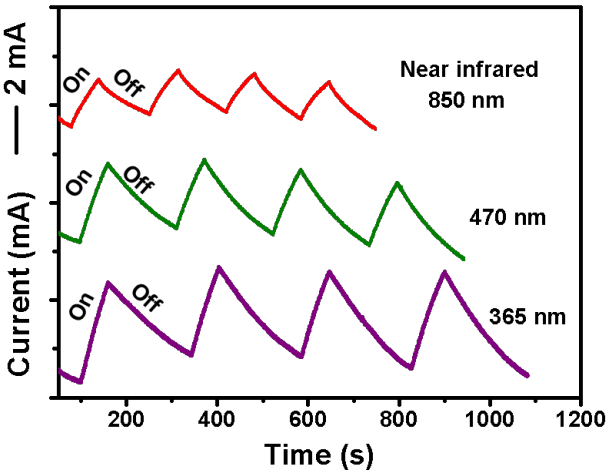

Fig. S25. Current response as a function of different wavelengths of light radiation for different cycles. The current increases when the light turns on and decreases when the light turns off. For each cycle, the light radiation duration is 60 s.

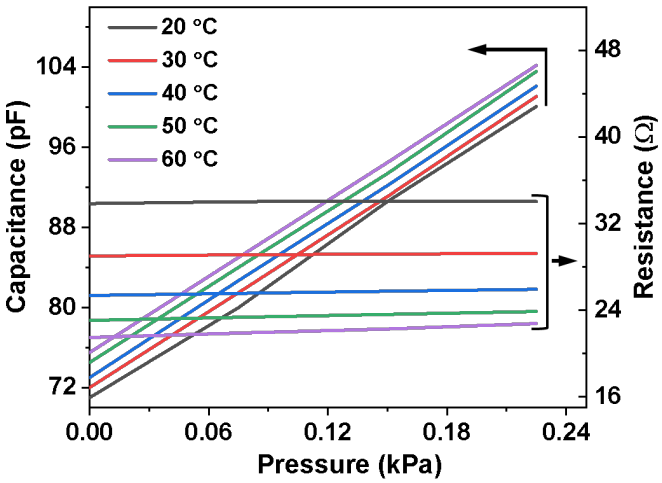

Fig. S26. The MXene-PpyNW-VSNP-PAM e-skin can discriminate mixed stimuli simultaneously.

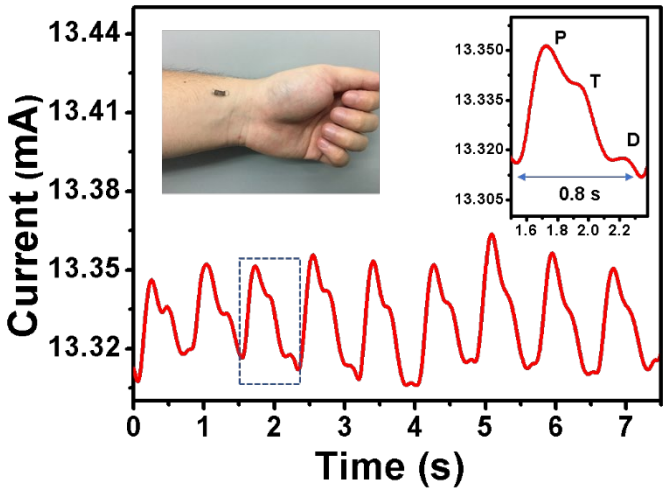

Fig. S27. Real-time and *in situ* human wrist arterial pulse waveforms measurement with the MXene-PpyNW-VSNP-PAM based e-skin sensor attached on the wrist of a test subject (Inset) with an applied voltage of 1V. The right panel shows a zoomed-in tracing of a representative waveform (blue dashed square). (Photo credit: Yichen Cai, and Jie Shen, KAUST)

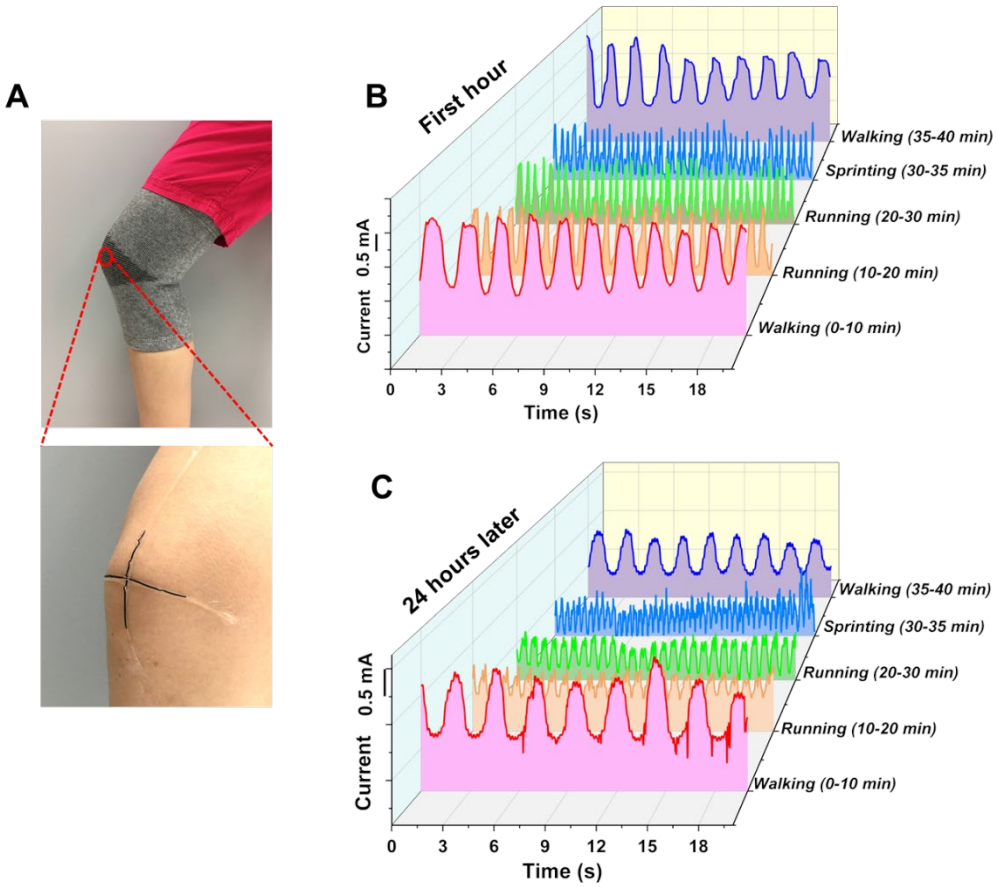

Fig. S28. Long-term performance during exercise studies for an e-skin sensor. (A) Photographs of the smart knee support with an integrated MXene-PpyNW-VSNP-PAM e-skin. (B) Monitoring of changes in electrical current during an exercise starting from warming up till the end of a workout with the duration of an hour. Distinguishable and repeatable patterns characteristic to specific exercises can be differentiated and systematically monitored after a long interval of 24 hours (C). (Photo credit: Yichen Cai, and Jie Shen, KAUST)

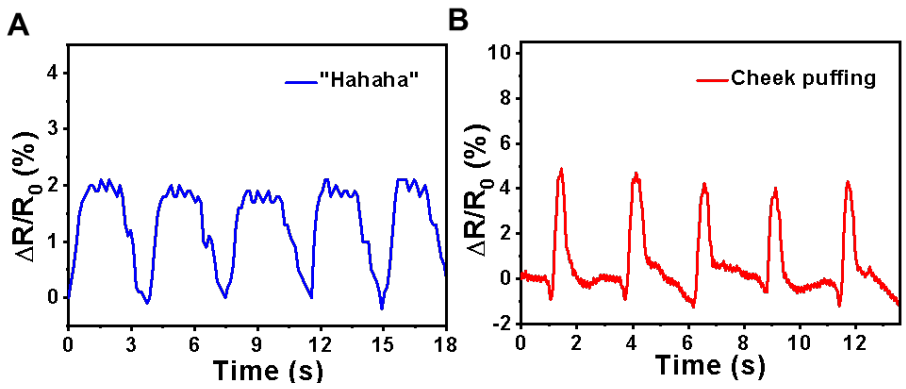

Fig. S29. Sensing nuance change in facial expressions. Sensing performance of the pressure sensor mounted onto the cheek of a volunteer for real-time sensing of laughing (A) and cheek puffing (B). By mounting the stretchable sensors on the cheek of volunteers, small facial muscle movements can be detected easily when the subjects laugh and or puff cheeks as is evident by the highly repeatable changes in the relative resistance of the sensor with high signal-to-noise ratios (Fig. S29A, B).

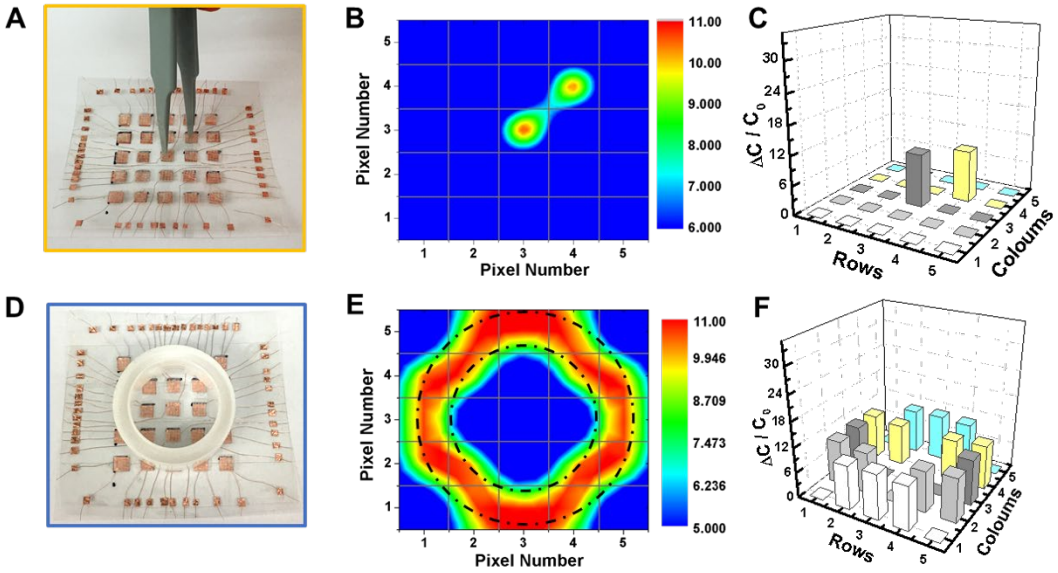

Fig. S30. Integrated e-skin with the effective dimensions of 3.0 cm × 3.0 cm assembled from the capacitive arrays is capable of detecting and mapping the distribution of various tactile signals and spatial pressures. (**A**) A photograph of "Point" stresses applied with a pair of tweezers. (Photo credit: Yichen Cai, and Jie Shen, KAUST) (**B**) Corresponding stress distribution mapping and (**C**) capacitance variation histogram for "Points". (**D**) Photograph of "Plane" stresses applied with a circular tape dispenser. (**E**) The stress distribution mapping matches the outline of the "plane". (Photo credit: Yichen Cai, and Jie Shen, KAUST) (**F**) Corresponding capacitance variation histogram. When a pair of tweezers is used to tap the sensor surface, local strains associated with points of contact were recognized. This is due to the fact that real-time output capacitor intensity of the sensor hinges on specific locations of contact (Fig. S30 A-C). Closely allied to the point mode, the multidimensional tactile sensing image when a circular tape dispenser was placed directly on the sensing arrays are shown in Fig. S30D. The resulting capacitance change and the color contrast mapping of the force distribution mesh well with the hollow shape of the circular tape dispenser (Fig. S30 E, F). This again underscores the potential of MXene-PpyNW-VSNP-PAM sensing arrays that could be used for simultaneous spatial mapping of exerted pressure in distributions and locations.

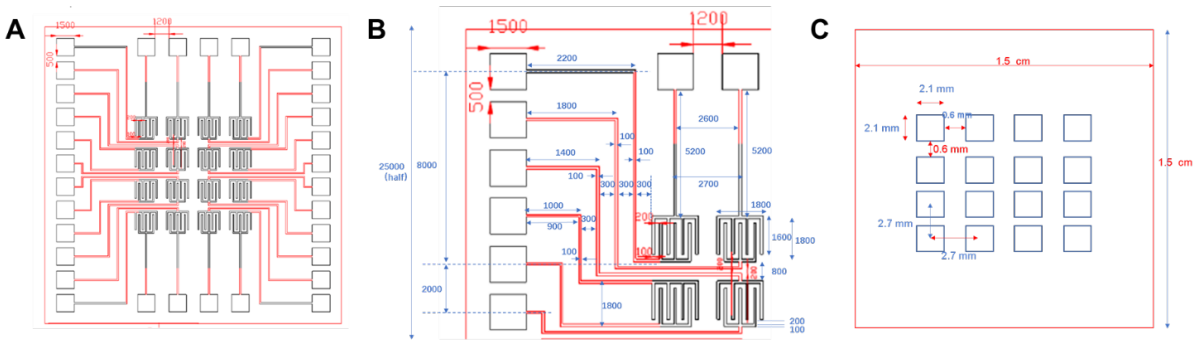

Fig. S31. Designs of shadow mask patterns for the printing of (**A**) interdigitated electrode arrays. (**B**) A close-up view reveals detailed dimensions of the interdigitated electrode arrays. (**C**) An array of squared openings for the interconnects.

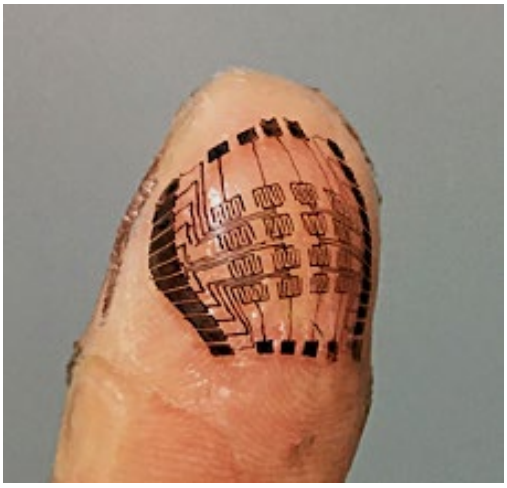

Fig. S32. **All-printable e-skins**. Demonstration of an array of electrodes using a shadow mask assisted spraying of MXene-PpyNW for both interdigital electrodes and interconnecting components. The fully flexible electrode arrays can be conformally adhered to the curvilinear surfaces of the thumb. (Photo credit: Yichen Cai, and Jie Shen, KAUST)

REFERENCES AND NOTES

1. S. Wang, J. Xu, W. Wang, G.-J. N. Wang, R. Rastak, F. Molina-Lopez, J. W. Chung, S. Niu, V. R. Feig, J. Lopez, T. Lei, S.-K. Kwon, Y. Kim, A. M. Foudeh, A. Ehrlich, A. Gasperini, Y. Yun, B. Murmann, J. B.-H. Tok, Z. Bao, Skin electronics from scalable fabrication of an intrinsically stretchable transistor array. *Nature* **555**, 83–88 (2018).

2. C. Larson, B. Peele, S. Li, S. Robinson, M. Totaro, L. Beccai, B. Mazzolai, R. Shepherd, Highly stretchable electroluminescent skin for optical signaling and tactile sensing. *Science* **351**, 1071–1074 (2016).

3. W. Gao, S. Emaminejad, H. Y. Y. Nyein, S. Challa, K. Chen, A. Peck, H. M. Fahad, H. Ota, H. Shiraki, D. Kiriya, D.-H. Lien, G. A. Brooks, R. W. Davis, A. Javey, Fully integrated wearable sensor arrays for multiplexed in situ perspiration analysis. *Nature* **529**, 509–514 (2016).

4. M. A. McEvoy, N. Correll, Materials that couple sensing, actuation, computation, and communication. *Science* **347**, 1261689 (2015).

5. C.-C. Kim, H.-H. Lee, K. H. Oh, J.-Y. Sun, Highly stretchable, transparent ionic touch panel. *Science* **353**, 682–687 (2016).

6. H. Yuk, T. Zhang, G. A. Parada, X. Liu, X. Zhao, Skin-inspired hydrogel–elastomer hybrids with robust interfaces and functional microstructures. *Nat.Commun.* **7**, 12028 (2016).

7. Z. Zhou, J. Liu, X. Zhang, D. Tian, Z. Zhan, C. Lu, Ultrathin MXene/calcium alginate aerogel film for high-performance electromagnetic interference shielding. *Adv. Mater. Interfaces* **6**, 1802040 (2019).

8. L.-X. Liu, W. Chen, H.-B. Zhang, Q.-W. Wang, F. Guan, Z.-Z. Yu, Flexible and multifunctional silk textiles with biomimetic leaf-like MXene/silver nanowire nanostructures for electromagnetic interference shielding, humidity monitoring, and self-derived hydrophobicity. *Adv. Funct. Mater.* **29**, 1905197 (2019).

9. X. Tang, D. Zhou, P. Li, X. Guo, B. Sun, H. Liu, K. Yan, Y. Gogotsi, G. Wang, MXene-based dendrite-free potassium metal batteries. *Adv. Mater.* **32**, 1906739 (2020).

10. J. Yang, W. Bao, P. Jaumaux, S. Zhang, C. Wang, G. Wang, MXene-based composites: Synthesis and applications in rechargeable batteries and supercapacitors. *Adv. Mater. Interfaces* **6**, 1802004 (2019).

11. J. Sun, W. Kong, Z. Jin, Y. Han, L. Ma, X. Ding, Y. Niu, Y. Xu, Recent advances of MXene as promising catalysts for electrochemical nitrogen reduction reaction. *Chinese Chem. Lett.* **31**, 953–960 (2020).

12. G. Monastyreckis, L. Mishnaevsky Jr, C. Hatter, A. Aniskevich, Y. Gogotsi, D. Zeleniakiene, Micromechanical modeling of MXene-polymer composites. *Carbon* **162**, 402–409 (2020).

13. A. Lipatov, H. Lu, M. Alhabeb, B. Anasori, A. Gruverman, Y. Gogotsi, A. Sinitskii, Elastic properties of 2D $Ti_3C_2T_x$ MXene monolayers and bilayers. *Sci. Adv.* **4**, 0491 (2018).

14. R. Li, L. Zhang, L. Shi, P. Wang, MXene Ti_3C_2: An effective 2D light-to-heat conversion material. *ACS Nano* **11**, 3752–3759 (2017).

15. K. Hantanasirisakul, Y. Gogotsi, Electronic and optical properties of 2D transition metal carbides and nitrides (MXenes). *Adv. Mater.* **30**, 1804779 (2018).

16. H. Liao, X. Guo, P. Wan, G. Yu, Conductive MXene nanocomposite organohydrogel for flexible, healable, low-temperature tolerant strain sensors. *Adv. Funct. Mater.* **29**, 1904507 (2019).

17. Y.-Z. Zhang, K. H. Lee, D. H. Anjum, R. Sougrat, Q. Jiang, H. Kim, H. N. Alshareef, MXenes stretch hydrogel sensor performance to new limits. *Sci. Adv.* **4**, eaat0098 (2018).

18. M. Wang, Y. Chen, R. Khan, H. Liu, C. Chen, T. Chen, R. Zhang, H. Li, A fast self-healing and conductive nanocomposite hydrogel as soft strain sensor. *Colloids Surf. A Physicochem. Eng. Asp.* **567**, 139–149 (2019).

19. G. Cai, J. Wang, K. Qian, J. Chen, S. Li, P. S. Lee, Extremely stretchable strain sensors based on conductive self-healing dynamic cross-links hydrogels for human-motion detection. *Adv. Sci.* **4**, 1600190 (2017).

20. X. Jiang, T. Jiang, X. Zhang, H. Dai, The plasticizing effect of calcium nitrate on poly(vinyl alcohol). *Polym. Eng. Sci.* **53**, 1181–1186 (2013).

21. Z. Wang, C. Xiang, X. Yao, P. Le Floch, J. Mendez, Z. Suo, Stretchable materials of high toughness and low hysteresis. *Proc. Natl. Acad. Sci. U.S.A.* **116**, 5967–5972 (2019).

22. C. H. Yang, B. Chen, J. Zhou, Y. M. Chen, Z. Suo, Electroluminescence of giant stretchability. *Adv. Mater.* **28**, 4480–4484 (2016).

23. Z. Jiang, B. Diggle, I. C. Shackleford, L. A. Connal, Tough, self-healing hydrogels capable of ultrafast shape changing. *Adv. Mater.* **31**, 1904056 (2019).

24. G. Lake, A. Thomas, The strength of highly elastic materials. *Proc. R. Soc. Lond. A* **300**, 108–119 (1967).

25. Y. Ma, N. Liu, L. Li, X. Hu, Z. Zou, J. Wang, S. Luo, Y. Gao, A highly flexible and sensitive piezoresistive sensor based on MXene with greatly changed interlayer distances. *Nat. Commun.* **8**, 1207 (2017).

26. Y. Cai, J. Shen, G. Ge, Y. Zhang, W. Jin, W. Huang, J. Shao, J. Yang, X. Dong, Stretchable $Ti_3C_2T_x$ MXene/carbon nanotube composite based strain sensor with ultrahigh sensitivity and tunable sensing range. *ACS Nano* **12**, 56–62 (2018).

27. J. Fang, P. Li, X. Lu, L. Fang, X. Lü, F. Ren, A strong, tough, and osteoconductive hydroxyapatite mineralized polyacrylamide/dextran hydrogel for bone tissue regeneration. *Acta Biomater.* **88**, 503–513 (2019).

28. H. Yuk, C. E. Varela, C. S. Nabzdyk, X. Mao, R. F. Padera, E. T. Roche, X. Zhao, Dry double-sided tape for adhesion of wet tissues and devices. *Nature* **575**, 169–174 (2019).

29. J. Steck, J. Yang, Z. Suo, Covalent topological adhesion. *ACS Macro Lett.* **8,** 754–758 (2019).

30. J. Yang, R. Bai, B. Chen, Z. Suo, Hydrogel adhesion: A supramolecular synergy of chemistry, topology, and mechanics. *Adv. Funct. Mater.* **30**, 1901693 (2019).

31. J. Cao, C. Lu, J. Zhuang, M. Liu, X. Zhang, Y. Yu, Q. Tao, Multiple hydrogen bonding enables the self-healing of sensors for human–machine interactions. *Angew. Chem. Int. Ed.* **56**, 8795–8800 (2017).

32. Z. Liu, X. Wang, D. Qi, C. Xu, J. Yu, Y. Liu, Y. Jiang, B. Liedberg, X. Chen, High-adhesion stretchable electrodes based on nanopile interlocking. *Adv. Mater.* **29**, 1603382 (2017).

33. S. Huang, Y. Liu, Y. Zhao, Z. Ren, C. F. Guo, Flexible electronics: Stretchable electrodes and their future. *Adv. Funct. Mater.* **29**, 1805924 (2019).

34. J.-Y. Sun, X. Zhao, W. R. Illeperuma, O. Chaudhuri, K. H. Oh, D. J. Mooney, J. J. Vlassak, Z. Suo, Highly stretchable and tough hydrogels. *Nature* **489**, 133–136 (2012).

35. X. Shi, H. Wang, X. Xie, Q. Xue, J. Zhang, S. Kang, C. Wang, J. Liang, Y. Chen, Bioinspired ultrasensitive and stretchable MXene-based strain sensor via nacre-mimetic microscale "brick-and-mortar" architecture. *ACS Nano* **13**, 649–659 (2018).

36. K. Tian, J. Bae, S. E. Bakarich, C. Yang, R. D. Gately, G. M. Spinks, M. in het Panhuis, Z. Suo, J. J. Vlassak, 3D printing of transparent and conductive heterogeneous hydrogel–elastomer systems. *Adv. Mater.* **29**, 1604827 (2017).

37. S. Y. Kim, S. Park, H. W. Park, D. H. Park, Y. Jeong, D. H. Kim, Highly sensitive and multimodal all-carbon skin sensors capable of simultaneously detecting tactile and biological stimuli. *Adv. Mater.* **27**, 4178–4185 (2015).

38. X. Wang, Y. Gu, Z. Xiong, Z. Cui, T. Zhang, Silk-molded flexible, ultrasensitive, and highly stable electronic skin for monitoring human physiological signals. *Adv. Mater.* **26**, 1336–1342 (2014).

39. S. Park, H. Kim, M. Vosgueritchian, S. Cheon, H. Kim, J. H. Koo, T. R. Kim, S. Lee, G. Schwartz, H. Chang, Z. Bao, Stretchable energy-harvesting tactile electronic skin capable of differentiating multiple mechanical stimuli modes. *Adv. Mater.* **26**, 7324–7332 (2014).

40. M. Wang, Z. Yan, T. Wang, P. Cai, S. Gao, Y. Zeng, C. Wan, H. Wang, L. Pan, J. Yu, S. Pan, K. He, J. Lu, X. Chen,Gesture recognition using a bioinspired learning architecture that integrates visual data with somatosensory data from stretchable sensors. *Nat. Electron.* **3**, 563–570 (2020).

41. Y. Huang, M. Zhong, Y. Huang, M. Zhu, Z. Pei, Z. Wang, Q. Xue, X. Xie, C. Zhi, A self-healable and highly stretchable supercapacitor based on a dual crosslinked polyelectrolyte. *Nat. Commun.* **6**, 10310 (2015).

42. L. Han, L. Yan, K. Wang, L. Fang, H. Zhang, Y. Tang, Y. Ding, L.-T. Weng, J. Xu, J. Weng, Y. Liu, F. Ren, X. Lu, Tough, self-healable and tissue-adhesive hydrogel with tunable multifunctionality. *NPG Asia Mater.* **9**, e372 (2017).

43. D. Zhang, X. Zhang, Y. Chen, P. Yu, C. Wang, Y. Ma, Enhanced capacitance and rate capability of graphene/polypyrrole composite as electrode material for supercapacitors. *J. Power Sources* **196**, 5990–5996 (2011).

44. L. Ding, Y. Wei, L. Li, T. Zhang, H. Wang, J. Xue, L.-X. Ding, S. Wang, J. Caro, Y. Gogotsi, MXene molecular sieving membranes for highly efficient gas separation. *Nat. Commun.* **9**, 155 (2018).

45. X. Yan, Z. Liu, Q. Zhang, J. Lopez, H. Wang, H.-C. Wu, S. Niu, H. Yan, S. Wang, T. Lei, J. Li, D. Qi, P. Huang, J. Huang, Y. Zhang, Y. Wang, G. Li, Jeffery B-H Tok, X. Chen, Z. Bao, Quadruple H-bonding cross-linked supramolecular polymeric materials as substrates for stretchable, antitearing, and self-healable thin film electrodes. *J. Am. Chem. Soc.* **140**, 5280–5289 (2018).

46. S. He, F. Zhang, S. Cheng, W. Wang, Synthesis of sodium acrylate and acrylamide copolymer/GO hydrogels and their effective adsorption for Pb^{2+} and Cd^{2+}. *ACS. Sustainable Chem. Eng.* **4**, 3948–3959 (2016).

47. M. Zhu, Y. Huang, Q. Deng, J. Zhou, Z. Pei, Q. Xue, Y. Huang, Z. Wang, H. Li, Q. Huang, C. Zi, Highly flexible, freestanding supercapacitor electrode with enhanced performance obtained by hybridizing polypyrrole chains with MXene. *Adv. Energ. Mater.* **6**, 1600969 (2016).

48. C. J. Zhang, S. Pinilla, N. McEvoy, C. P. Cullen, B. Anasori, E. Long, S.-H. Park, A. S. Seral-Ascaso, A. Shmeliov, D. Krishnan, C. Morant, X. Liu, G. S. Duesderg, Y. Gogotsi, V. Nicolosi,

Oxidation stability of colloidal two-dimensional titanium carbides (MXenes). *Chem. Mater.* **29**, 4848–4856 (2017).

49. L. Ding, Y. Wei, Y. Wang, H. Chen, J. Caro, H. Wang, A two-dimensional lamellar membrane: MXene nanosheet stacks. *Angew. Chem. Int. Ed.* **56**, 1825–1829 (2017).

50. Y.-J. Liu, W.-T. Cao, M.-G. Ma, P. Wan, Ultrasensitive wearable soft strain sensors of conductive, self-healing, and elastic hydrogels with synergistic "soft and hard" hybrid networks. *ACS Appl. Mater. Interfaces* **9**, 25559–25570 (2017).

51. J. M. González-Domínguez, C. Martín, O. S. J. Durá, S. Merino, E. Vázquez, Smart hybrid graphene hydrogels: A study of the different responses to mechanical stretching stimulus. *ACS Appl. Mater. Interfaces* **10**, 1987–1995 (2018).

52. S. Liu, L. Li, Ultrastretchable and self-healing double-network hydrogel for 3D printing and strain sensor. *ACS Appl. Mater. Interfaces* **9**, 26429–26437 (2017).

53. Z. Lei, Q. Wang, S. Sun, W. Zhu, P. Wu, A bioinspired mineral hydrogel as a self-healable, mechanically adaptable ionic skin for highly sensitive pressure sensing. *Adv. Mater.* **29**, 1700321 (2017).

54. F. Lin, Z. Wang, Y. Shen, L. Tang, P. Zhang, Y. Wang, Y. Chen, B. Huang, B. Lu, Natural skin-inspired versatile cellulose biomimetic hydrogels. *J. Mater. Chem. A* **7**, 26442–26455 (2019).

55. X. Wang, T. Li, J. Adams, J. Yang, Transparent, stretchable, carbon-nanotube-inlaid conductors enabled by standard replication technology for capacitive pressure, strain and touch sensors. *J. Mater. Chem. A* **1**, 3580–3586 (2013).